

Journal of Biomedical Optics

BiomedicalOptics.SPIEDigitalLibrary.org

Macroscopic-imaging technique for subsurface quantification of near-infrared markers during surgery

Michael Jermyn
Kolbein Kolste
Julien Pichette
Guillaume Sheehy
Leticia Angulo-Rodríguez
Keith D. Paulsen
David W. Roberts
Brian C. Wilson
Kevin Petrecca
Frederic Leblond

Macroscopic-imaging technique for subsurface quantification of near-infrared markers during surgery

Michael Jermyn,^{a,b} Kolbein Kolste,^c Julien Pichette,^b Guillaume Sheehy,^b Leticia Angulo-Rodríguez,^b Keith D. Paulsen,^c David W. Roberts,^d Brian C. Wilson,^e Kevin Petrecca,^a and Frederic Leblond^{b,*}

^aMcGill University, Brain Tumour Research Centre, Montreal Neurological Institute and Hospital, Department of Neurology and Neurosurgery, 3801 University Street, Montreal, Quebec H3A 2B4, Canada

^bPolytechnique Montreal, Department of Engineering Physics, CP 6079, Succ. Centre-Ville, Montreal, Quebec H3C 3A7, Canada

^cDartmouth College, Thayer School of Engineering, 14 Engineering Drive, Hanover, New Hampshire 03755, United States

^dDartmouth-Hitchcock Medical Center, Section of Neurosurgery, Lebanon, New Hampshire 03756, United States

^eUniversity of Toronto/University Health Network, Department of Medical Biophysics, 101 College Street, Toronto, Ontario M5G 1L7, Canada

Abstract. Obtaining accurate quantitative information on the concentration and distribution of fluorescent markers lying at a depth below the surface of optically turbid media, such as tissue, is a significant challenge. Here, we introduce a fluorescence reconstruction technique based on a diffusion light transport model that can be used during surgery, including guiding resection of brain tumors, for depth-resolved quantitative imaging of near-infrared fluorescent markers. Hyperspectral fluorescence images are used to compute a topographic map of the fluorophore distribution, which yields structural and optical constraints for a three-dimensional subsequent hyperspectral diffuse fluorescence reconstruction algorithm. Using the model fluorophore Alexa Fluor 647 and brain-like tissue phantoms, the technique yielded estimates of fluorophore concentration within $\pm 25\%$ of the true value to depths of 5 to 9 mm, depending on the concentration. The approach is practical for integration into a neurosurgical fluorescence microscope and has potential to further extend fluorescence-guided resection using objective and quantified metrics of the presence of residual tumor tissue. © 2015 Society of Photo-Optical Instrumentation Engineers (SPIE) [DOI: 10.1117/1.JBO.20.3.036014]

Keywords: fluorescence; neurosurgery; optical reconstruction; near-infrared; diffusion.

Paper 150021R received Jan. 14, 2015; accepted for publication Mar. 3, 2015; published online Mar. 20, 2015.

1 Introduction

Modalities such as magnetic resonance imaging (MRI) and x-ray computed tomography (CT) enable tumor detection and surgical planning for patients with brain cancer, so that the surgeon then navigates through a combination of visual cues from the surgical field and these coregistered images. However, residual tumor frequently remains following surgery, and reducing the volume of this unresected tissue has a significant impact on progression-free and overall survival of glioma patients.¹⁻⁴ Various optical imaging and spectroscopy techniques, beyond the white-light operating microscope, have been developed to enhance intraoperative guidance by providing increased sensitivity and specificity to the presence of malignant tissue in the surgical field.⁵⁻⁹ Fluorescence-guided surgery using protoporphyrin IX (PpIX) that is endogenously synthesized in tumor cells following systemic (e.g., oral) administration of 5-aminolevulinic acid (5-ALA) has demonstrated significant survival benefits for glioblastoma patients.¹⁰⁻¹⁴ In previous work, we have shown that fluorescence and reflectance point spectroscopy can be used for quantitative fluorescence (qF) measurements, where the tissue absorption and scattering spectra are derived from the diffuse reflectance spectrum and then used to correct the measured fluorescence spectrum for the effects of wavelength-dependent attenuation of the excitation and emission light.^{14,15} The efficacy of this approach in

increasing the sensitivity and specificity of residual tumor detection compared with qualitative visualization of the fluorescence has been reported for several different types of intracranial tumors,^{13,15} and multicenter clinical trials are currently underway. The accuracy for quantifying the local fluorophore concentration in tissue is $\pm 10\%$ for PpIX levels down to ~ 10 ng/ml. Subsequently, we have reported initial studies extending this concept to wide-field quantitative fluorescence imaging (qFI), where the fluorophore concentration is estimated at every point (pixel) on the tissue surface in the surgical field-of-view,^{14,16,17} and have shown that it enables imaging of clinically relevant fluorescence that is below the detection threshold of standard visually evaluated fluorescence imaging through the neurosurgical microscope.

The availability of other tumor-specific fluorescent contrast agents for human use has been a limitation in general for fluorescence-guided surgery, but new near-infrared (NIR) probes are being developed by several groups for this purpose, so that extending qFI into the NIR domain is likely to be of value.^{18,19} The use of NIR light is advantageous because it can penetrate up to several centimeters into biological tissue, allowing detection of molecular targets lying below the immediate surgical resection surface.

As indicated above, quantitative fluorescence-guided surgery is confounded by the interplay of heterogeneous tissue attenuation with the variable depths and concentrations of potential fluorescent sources.²⁰ Thus, for example, it is challenging to

*Address all correspondence to: Frederic Leblond, E-mail: frederic.leblond@polymtl.ca

distinguish between a high concentration of fluorophore at depth and a low concentration near the tissue surface. In general, diffuse optical tomographic methods can be combined with structural information from preoperative imaging modalities (such as CT, MRI, or ultrasound) in order to improve the performance (optical contrast, spatial localization) of subsurface reconstruction.^{21–24} However, for most surgical guidance applications, tomography techniques have to be implemented in an epi-illumination geometry rather than using transillumination of the tissue volume.^{23,25–27} Hence, the fluorescence images are heavily surface-weighted.²⁸ Fluorescence molecular tomography (FMT) with an array of light source-detector pairs that sample multiple photon paths can be used to improve subsurface quantification,^{28,29} in some cases exploiting photon time-of-flight acquisition to increase the accuracy of the recovered fluorescence concentration.^{30–33} However, FMT is not easily implemented into a neurosurgical microscope and is extremely sensitive to instrumentation alignment. Studies have demonstrated the inability of fluorescence tomography to be quantitative at depth due to the effects of fluorescence depth sensitivity and fluorophore concentration.^{34,35} Kepshire et al. investigated the use of FMT for subsurface fluorescence imaging, with errors >50% in recovered fluorescence concentration for depths >4 mm, even for higher fluorophore concentrations.³⁶ A need exists for depth-resolved quantitative fluorescence imaging that can be easily integrated into the established neurosurgical environment. The ability to both localize and quantify residual cancer beneath the immediate surface of the surgical cavity could reduce the volume of tumor remaining after surgery and thus, improve intermediate and potentially the long-term survival.

To address this clinical need, we report here a technique for depth-resolved quantitative reconstruction of NIR fluorescent markers that is integrated into a commercial neurosurgical microscope. Quantitative reconstruction at depth uses a novel two-step algorithm. First, the effective fluorophore depth of each image pixel is estimated using the ratio of the fluorescence intensity at two emission wavelengths,¹⁷ exploiting the distortion (redshift) of the detected fluorescence spectrum due to depth-dependent attenuation of the emitted fluorescent light.^{13,17} This depth information is then used as a prior spatial constraint to reduce the ill-posed nature of the inversion procedure of the second step, in which a three-dimensional (3-D) hyperspectral fluorescence reconstruction algorithm separates the convolved effects of fluorophore depth and concentration in order to maximize the accuracy of the reconstruction.^{9,37–40} While the application presented here is focused on neurosurgery, the algorithm is broadly applicable to fluorescence-guided resection using NIR fluorescent markers.

2 Materials and Methods

2.1 Quantitative Fluorescence Image Reconstruction

2.1.1 Depth estimation using spectral distortion

Separating the fluorophore depth and concentration is critical for accurate quantitative subsurface fluorescence recovery. It has been shown that the logarithm of the ratio of fluorescence intensities detected at two different wavelengths,¹⁷ Γ , varies approximately linearly with fluorophore depth (with Γ defined as the ratio of the intensity at the longer wavelength divided by the intensity at the shorter wavelength). Thus, an estimate of the effective fluorophore depth, d , at each image pixel is given by¹⁷

$$d = \frac{\ln(\Gamma) - \ln\left(\frac{D^{\lambda_2}}{D^{\lambda_1}}\right)}{\left(\frac{1}{\delta^{\lambda_2}} - \frac{1}{\delta^{\lambda_1}}\right)}, \quad (1)$$

where D^{λ_1} and D^{λ_2} are the diffusion coefficients at the selected wavelengths ($\lambda_2 > \lambda_1$) used for Γ and δ^{λ_1} and δ^{λ_2} are the corresponding effective penetration depths, given by⁴¹

$$D = \frac{1}{3(\mu_a + \mu'_s)}, \quad (2)$$

$$\delta = \sqrt{\frac{D}{\mu_a}}, \quad (3)$$

where μ_a is the absorption coefficient and μ'_s is the reduced scattering coefficient. These computed d values correspond to an effective depth which depends on the optical sensitivity and the true fluorescence distribution. We recently showed in tissue-simulating phantoms that fluorescence ratio images, combined with the use of Eq. (1), generated topographic maps of NIR fluorophore distribution for depths of up to several millimeters.⁴²

2.1.2 Forming fluorescence topography maps to constrain image reconstruction

The above fluorophore depth information is used as a spatial constraint in the 3-D hyperspectral fluorescence reconstruction algorithm, as described below. However, as recently demonstrated,⁴² these effective depth values may be compromised in regions of low fluorophore signal relative to the tissue autofluorescence background or ambient light leakage. Hence, we apply a threshold, d_t , equal to the mean effective depth across the field-of-view to obtain the most robust region of positive fluorescence signal, assuming, of course, that the fluorophore concentration in tumor is higher than in normal surrounding tissue. This threshold, d_t , is the mean of the d values from Eq. (1) across all image pixels in the field of view. The d values are estimates of fluorophore depth at each pixel, so the threshold will depend on the inclusion depth and topography near the tissue surface, allowing us to exclude depth values that do not correspond to the fluorescence inclusion. Regions in the field-of-view in which $d < d_t$ are not used in constraining the hyperspectral fluorescence reconstruction. The remaining depth map ($d \geq d_t$) is then referred to as the partial topography of the tumor, T_{pt} . This represents the dominant regions of high fluorophore concentration and is considered a first approximation to the subsurface tumor region. Henceforth in this work, all depth estimates are made using the wavelength pair $\lambda_1 = 670$ nm and $\lambda_2 = 720$ nm, which were found to provide the most robust depth estimates using PpIX for a range of bulk optical properties consistent with brain tissue, as demonstrated in Ref. 42.

2.1.3 Constrained 3-D hyperspectral fluorescence reconstruction algorithm

A 3-D hyperspectral fluorescence reconstruction method was then developed that incorporates T_{pt} as a constraint as follows. First, a 3-D tetrahedral volume mesh is constructed representing the interrogated tissue domain. A diffuse-light transport model is then applied iteratively to find the best fit between the experimental data and the model-based predictions for the hyperspectral fluorescence images. At each iteration, the latter are made

using numerical solutions to the diffusion equations based on the finite-element code NIRFAST,⁴³ with the bulk optical properties (absorption and reduced scattering) fixed and varying the fluorophore concentration and distribution. Regularization was used in the optimization problem that comprises a modified Tikhonov minimization inverse-problem approach.⁴⁴

Seventeen wavelengths from 650 to 730 nm in 5 nm increments were used and the experimental bulk tissue optical properties (absorption and scattering) were used as input parameters in the diffusion model for optical reconstruction. The partial topography map, T_{pt} , served as a spatial prior to construct a Laplacian regularization matrix L ,⁴⁵ and the weight of the spatial priors can be varied throughout the tissue volume. Laplacian regularization uses the structural information about tissue in order to improve quantification in optical reconstruction. L is a filter matrix that affects the penalty term in the modified Tikhonov approach, using the structural information of tissue as smoothness constraints. The matrix encodes the relationship between each node in a mesh to all other nodes and uses these values to smooth predefined tissue structure. The addition of prior structural information has been shown to improve fluorescence concentration recovery in optical tomography.⁴⁵ Here we determine the entries of L from an estimated confidence map of the fluorescence spatial distribution that corresponds to the likelihood that a given location (mesh node) actually belongs to the subsurface inclusion (tumor). Thus, L alters the reconstruction to use the prior spatial information in order to more accurately recover the fluorescence distribution by specifying that certain regions (e.g., the tumor) are more likely to have similar fluorescence values.

2.1.4 Computing the elements of the constraint matrix L

The next step consists in making a semiempirical prediction about whether or not each voxel of the reconstructed volume belongs to the actual 3-D fluorescent volume. Specifically, for each node, n_i , in the tetrahedral mesh, a confidence value is defined quantifying the likelihood that the node is within the fluorescence inclusion, based on the T_{pt} coverage. Here the term coverage refers to whether or not the node is located beneath T_{pt} , which is determined as follows. First, a ray is generated from n_i to the closest illumination point on the tissue surface (Fig. 1). If the ray intersects T_{pt} , then the distance, k_i , between n_i and T_{pt} is computed. The k_i values are then normalized by the maximum across all nodes, so that k ranges from 0 to 1, and the smallest value is associated with elements closest to the inner boundaries of the partial surface. If no intersection occurs, a value of $k_i = 1$ is used; as shown below, this leads to a zero confidence that the node is within the fluorescent inclusion.

Near the edges of the depth map (near the boundary of the fluorescent inclusion), it is difficult to ascertain which areas are in the true fluorescence region and which are not. Light transport yields imprecise boundaries, making it challenging to delineate the inclusion border for spatial priors. In order to account for this, a value m_i is computed as follows for each node of nonzero confidence ($k_i < 1$) as a measure of whether it lies near the edge. For these nodes, their proximity to the edge of T_{pt} (as viewed from the tissue surface) is calculated by constructing a sphere S at the point of intersection between the ray and T_{pt} (Fig. 1). The radius of S was chosen to be four times the mesh edge length at

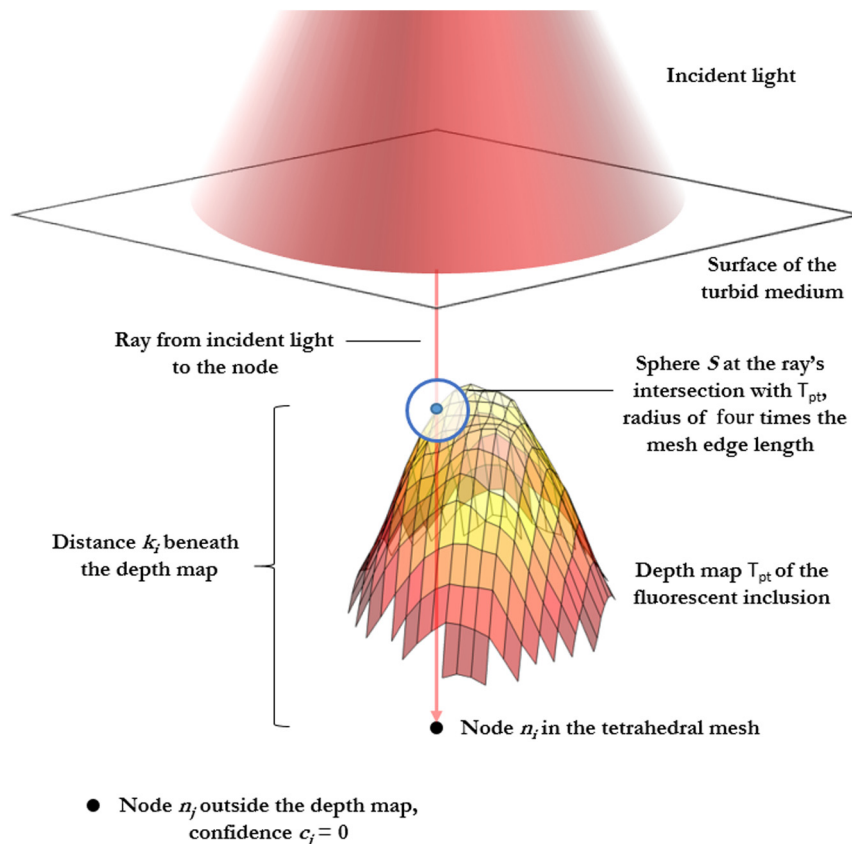


Fig. 1 Conceptual diagram illustrating the use of T_{pt} to determine the confidence that a particular mesh node is within the fluorescent inclusion.

that location, this being large enough to capture many points in T_{pt} while being sufficiently small so as to not oversmooth the estimate of the edge. m_i is the number of points within T_{pt} that are inside S ; a lower number will correspond to nodes closer to the edge of T_{pt} . The value for m_i is then normalized by its maximum across all nodes, so that m also ranges from 0 to 1. Intuitively, this corresponds to how much of the fluorescent inclusion surface is directly above the node relative to the incident light. The confidence, c_i , that a node, n_i , is in the fluorescence inclusion is calculated as

$$c_i = m_i(1 - k_i). \quad (4)$$

This represents the likelihood that a given node is within the fluorescent inclusion, based on the coverage of the fluorescence surface, and with a correction term m_i to account for positions near the boundary. The value for k_i represents the distance of a node from the depth map T_{pt} , normalized to vary from 0 to 1, so $(1 - k_i)$ will correspond to how close the node is to the depth map. We are, therefore, saying that nodes closer to the depth map have a higher confidence c_i of being in the fluorescent inclusion. Each regularization matrix element, $L_{i,j}$, for the pair of nodes n_i and n_j , is calculated as in Eq. (5):

$$L_{i,j} = \begin{cases} i = j: & 1 \\ c_i = c_j = 0: & -g_b^{-1} \\ c_i \neq c_j = 0: & 0 \\ c_j \neq c_i = 0: & 0 \\ c_i \neq 0 \neq c_j: & -c_i c_j g_f^{-1} \end{cases}, \quad (5)$$

$$g_b = \sum_{c_i=0} 1, \quad (6)$$

$$g_f = \sum_{c_i \neq 0} 1. \quad (7)$$

Here, g_b is the number of nodes with confidence c_i of 0, and g_f is the number of nodes with nonzero confidence c_i . These correspond to the expected number of nodes in the nonfluorescent region and fluorescent region, respectively. When two nodes are both in the nonfluorescent region [entry 2 of Eq. (5)], they are assigned a fixed value in L , resulting in homogenous smoothing across the nonfluorescent region. When two nodes are both in the fluorescent region [entry 5 of Eq. (5)], they are assigned a value based on the confidence for both nodes being in the fluorescent region. The more the confidence that both nodes are in the fluorescent region, the greater is the smoothing that will be applied. Therefore, nodes with high confidence of being in the fluorescent inclusion will be more likely to have similar fluorescence concentrations recovered. If two nodes are not in the same region [entries 3 and 4 of Eq. (5)], they are assigned a value of 0 in L and no smoothing occurs. The diagonal of L is 1 [entry 1 of Eq. (5)], corresponding to the relationship between a node and itself. This is the standard construction for the L matrix, with the fluorescent region incorporated as a scaling factor (based on the confidence c_i). Equation (5) implies that, for nodes likely to be in the fluorescent inclusion, the regularization matrix is scaled by the confidence, so that during the reconstruction, it will be more likely that the recovered fluorescence values for such nodes will be similar. Hence, L reduces the variation in recovered fluorescence

concentration within the fluorescent inclusion by assigning non-zero values to pairs of nodes that are in the same region.

Without the prior structural information from T_{pt} , the diffuse fluorescence reconstruction is ill-posed with multiple equivalent solutions. Using T_{pt} reduces the number of equivalent solutions by favoring those that are the most consistent with the geometry of the subsurface tumor and the actual concentration of fluorescent markers.

2.2 Tests in Tissue-Simulating Phantoms

The hyperspectral fluorescence imaging system [Fig. 2(a)] as described previously¹⁴ is integrated with a commercial neurosurgical microscope (Carl Zeiss Meditec) through a custom optical adapter (TrueTex) to ensure alignment of the fluorescence field-of-view with the standard microscope image. It comprises a liquid crystal tunable filter (LCTF; VIS-7-20, Varispec, Cri), a 650-nm longpass filter (ET650lp, Chroma), a 632-nm laser diode (7400 series, Intense Co.) for fluorescence excitation, and a CCD camera (PixelFlyUSB, PCO). The LCTF selects detection wavelengths from 650 to 720 nm with a 5-nm spectral resolution. A 635-nm bandpass filter (ZET635/20X EX, Chroma) and collimator (F220SMA-B, Thorlabs) reduce the bleed-through of excitation light to the detector.

A liquid phantom comprising 1% Intralipid (Intralipid 20%, Patterson Veterinary Supply), 0.4 mg/mL methemoglobin (H2500, SigmaAldrich), and water was created with optical properties of approximately $\mu_a = 0.001 \text{ mm}^{-1}$ and $\mu'_s = 1 \text{ mm}^{-1}$ at 700 nm, representative of brain tissue.¹⁵ Absorption was calculated based on literature values for the methemoglobin extinction coefficient,⁴⁶ and scattering was estimated from the concentration of Intralipid.⁴⁷ The phantom container was a cylinder 7 cm in diameter and 4 cm in height. The inclusion was also cylindrical (2 cm in diameter and 1 cm in height) and was filled with the same diffusive medium but with the addition of Alexa Fluor 647 (AF647) as a fluorophore. The inclusion was placed in the center of the larger container and diffusive liquid was added until flush with the top of the inclusion. A hyperspectral fluorescence image [Fig. 2(b)] was recorded in this position and referred to as the 0 mm depth. 3.85 mL of bulk liquid was incrementally added to increase the depth of the inclusion in 1-mm increments to a maximum depth of 10 mm. Bulk liquid was added based on the volume needed to increase the depth by 1-mm increments and was verified by ruler measurements.⁴² Images were acquired at each step. This was repeated for a range of AF647 concentrations (0.3125, 0.625, 1.25, 2.5, 5, and 10 $\mu\text{g/ml}$). All spectroscopic images were recorded with a total integration time of 2 s.

3 Results

The accuracy of the reconstruction algorithm was evaluated in phantom experiments for a range of fluorophore concentrations and inclusion depths, and Fig. 3 shows examples of the fluorescence-ratio images calculated from the phantom images for two different concentrations as a function of depth.

Figure 4 shows the corresponding surfaces representing the partial topography of the inclusion beneath the tissue surface, which provides the spatial priors for constraining the reconstruction. The recovered inclusion depths support previous work demonstrating millimeter accuracy for depths up to 5 to 10 mm.³⁹

The average of Γ in a 3×3 pixel window (pixel size on the surface $\sim 0.1 \text{ mm}$ at the center of the inclusion) was calculated and the expected linearity between $\ln(\Gamma)$ and inclusion depth

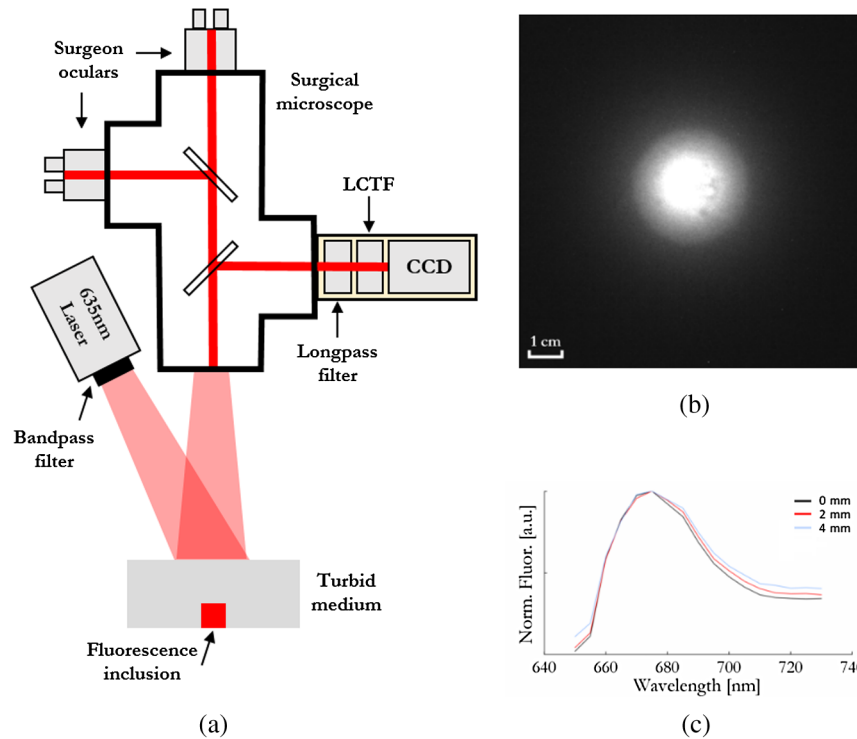


Fig. 2 (a) Schematic diagram of the hyperspectral fluorescence imaging system, (b) fluorescence emission image at a single wavelength of a phantom with a fluorescent inclusion, and (c) examples of detected fluorescence emission spectra for different inclusion depths (depth of top surface of inclusion), measured in a 3×3 pixel window at the center of the inclusion in the camera image and normalized to the maximum emission.

[Fig. 5(a)] and its independence of the fluorophore concentration was verified. The fluorophore concentration was then recovered with the constrained hyperspectral fluorescence reconstruction algorithm and compared with the true concentration to assess the accuracy of the method: this is summarized in Fig. 5(b), which shows the percentage error between these as a function of the inclusion depth. The recovered concentrations are presented alongside the depth maps in Fig. 6 and

demonstrate the ability to estimate the fluorophore concentration at varying depths. While Figs. 5 and 6 contain results for three concentrations of AF647, concentration estimates were determined for all six levels (0.3125, 0.625, 1.25, 2.5, 5, and $10 \mu\text{g/ml}$), and the estimation error was $<25\%$ for inclusion depths up to 5 mm beneath the phantom surface. Moreover, for concentrations $>2.5 \mu\text{g/ml}$, the estimation error was $<25\%$ for inclusion depths up to 9 mm.

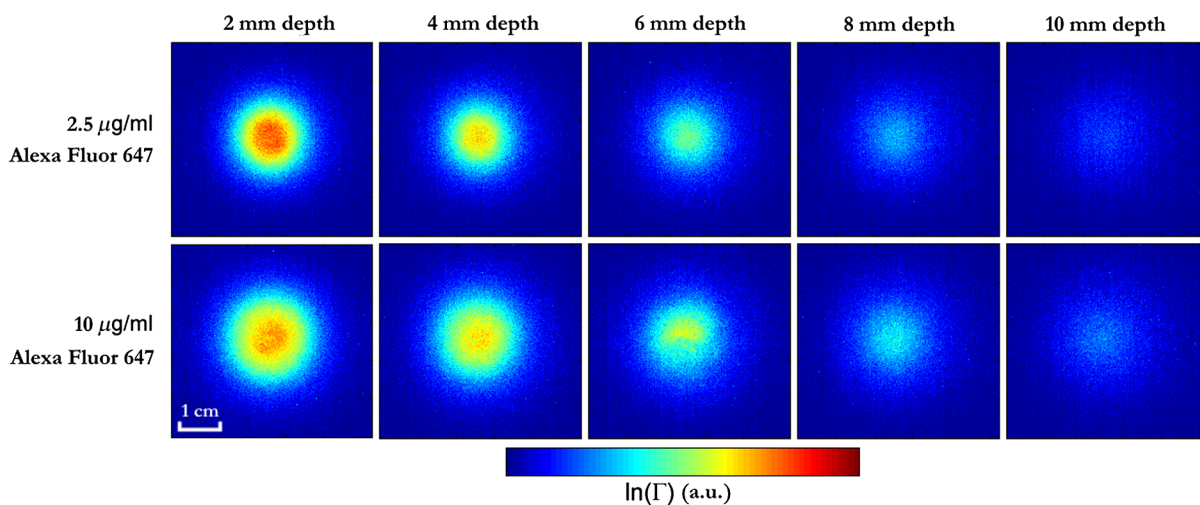


Fig. 3 The dual-wavelength fluorescence emission ratio over the camera image (cropped to an area in the vicinity of the inclusion), for two different concentrations of Alexa Fluor 647 and multiple inclusion depths (odd-valued depth values not shown).

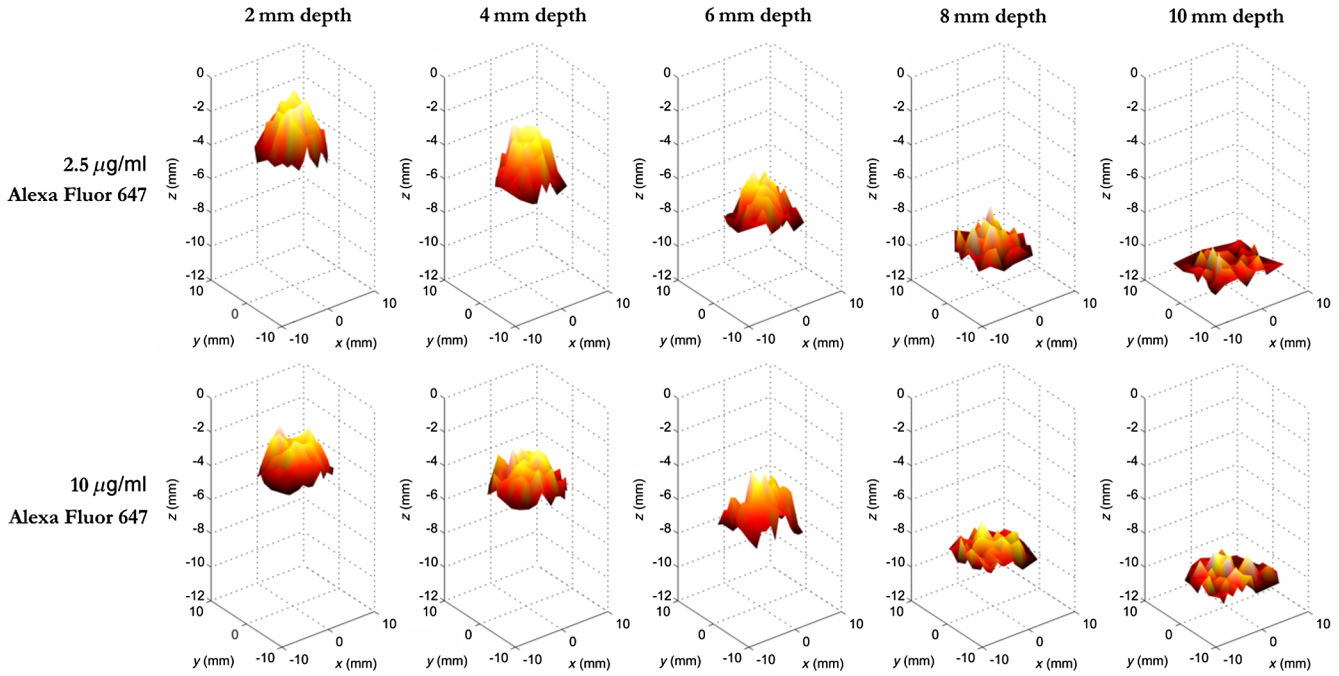


Fig. 4 Partial surfaces corresponding to Fig. 3, representing the first-stage estimate of the topography of the fluorescent inclusion beneath the tissue surface.

4 Discussion

The depth-dependent information from dual-wavelength fluorescence emission ratios [Fig. 3(a)] provides spatial priors which can be used to separate the effects of fluorophore depth and concentration in the diffuse-light reconstruction. The technique has been investigated in phantoms and the fluorophore concentration was recovered within $\pm 25\%$ for inclusion depths up to 5 mm beneath the surface for a range of concentrations between 0.3125 and 10.0 $\mu\text{g/ml}$ of AF647 [Fig. 3(b)]. For concentrations of 2.5 $\mu\text{g/ml}$ or greater, this accuracy was maintained to a 9 mm depth.

The reconstruction algorithm uses a diffusion-based light transport model, which has limitations when measurements associated with subdiffusive light paths are used ($< \sim 3$ to 5 reduced scattering lengths).^{44,48} Light transport models that are more accurate near the tissue surface, such as Monte Carlo

modeling,^{49,50} or higher-order solutions to radiation transport⁵¹ could further improve the ability to quantify fluorescence concentration, especially relatively near the tissue surface.

With biomarker-targeted fluorophores (e.g., antibody- or peptide-fluorophore conjugates), the strength of binding to the tumor cells/tissue may also limit the accuracy of this technique if a fraction of the marker does not bind to the target but instead generates a fluorescent background signal. Note that this is not a major concern using ALA-induced PpIX fluorescence, since the concentration of PpIX in normal brain, at least in white matter wherein most adult gliomas arise, is very low (typically $< 0.1 \mu\text{g/ml}$).¹⁵ The use of dual tracers that allow this background to be subtracted would address this issue as long as the detected signals are not limited by the dynamic range of the camera.⁵² The presence of significant endogenous (auto)fluorescence would likewise alter the contrast-to-background ratio and

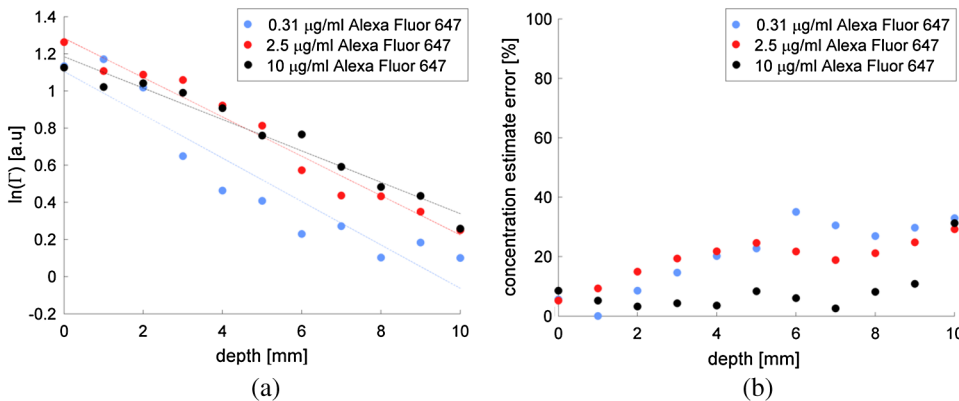


Fig. 5 Fluorescence quantification at depth from phantom measurements: (a) log of Γ versus inclusion depth for three different fluorophore concentrations, computed from a 3×3 pixel window in the center of the inclusion and (b) percentage error in the estimate for fluorophore concentration versus inclusion depth; the estimated concentration is based on the average value within the true inclusion region.

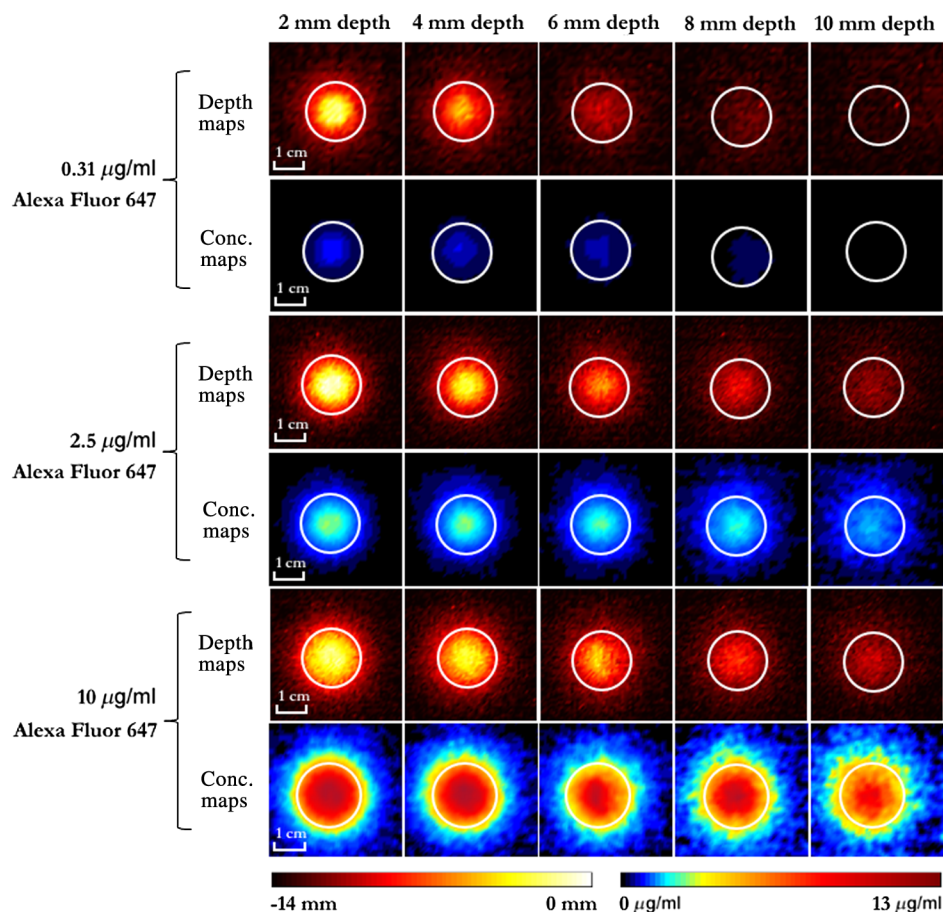


Fig. 6 Depth maps (in hot/red) show the result of using the dual-wavelength fluorescence emission ratio to determine the depth of fluorescence at each point in the camera image for the phantom (cropped to show the inclusion). Reconstructed concentration maps (in modified jet) are shown as the maximum intensity projection of the three-dimensional recovered concentration volume onto the two-dimensional tissue surface. The true boundary of the fluorescent inclusion is indicated by the white circle.

reduce the accuracy of the quantitative imaging of the administered fluorophore. This is of less concern in the use of NIR fluorophores, since tissue autofluorescence generally decreases in this region.

In the above phantom studies, uniform bulk tissue optical properties were used as the initial estimates in the optical reconstruction. Actual spatial mapping of the tissue absorption and transport scattering coefficients at the fluorescence excitation and emission wavelengths could be obtained from spatial light modulation imaging,^{53,54} which could be integrated onto the neurosurgical microscope. Alternatively, the previously reported point reflectance spectroscopy probe could be used to sample the tissue properties.¹⁵ Due to the diffuse nature of light transport in optically turbid media, blurring is observed toward the edges of fluorescence inclusions in the camera images. This, therefore, affects our estimates of fluorescence depth⁴² and, subsequently, the reconstructed fluorescence concentration maps. It will primarily limit the ability to delineate inclusion boundaries, rather than affect bulk fluorescence concentration and depth estimates. Studies have investigated the use of spectroscopic excitation data in combination with spectral emission to improve the ability to extract fluorescence depth information and reduce the ill-posedness of the inverse problem.^{40,55} This exploits the spectral depth dependency at the excitation wavelength range to provide more depth-dependent

information. It may be valuable to explore the use of excitation spectroscopy in combination with the proposed technique for improved quantification of fluorescence at depth.

In conclusion, we have demonstrated that the two-step reconstruction algorithm is able to map fluorescence concentration at depth with an accuracy that is likely to be clinically useful, depending on the tumor localization properties of the particular fluorophore used.^{39,56,57} The information could be presented to the surgeon as in Fig. 6, with one map showing the fluorophore depth distribution and the other indicating the fluorescence concentration at that depth. The depth information would then be used by the surgeon to decide if it is technically possible and safe to continue resection, while the concentration would serve as a metric of the probability of the fluorescence being tumor-associated: for example, multicenter clinical trials are in progress using our point spectroscopy probe instrument to determine the relationship between tumor probability and measured PpIX concentration. These depth and concentration maps could be overlaid with the view from the operating microscope for easy integration with surgical workflow. Residual and resectable cancer tissue can extend beyond what is delineated by the current standard-of-care (visual inspection and coregistered MRI), leading to recurrence and negatively impacting patient outcomes. This situation has been improved by the introduction of intraoperative fluorescence imaging. However, the current

approach using subjective interpretation of qualitative fluorescence images is suboptimal and the added capabilities to both determine the depth of any subsurface residual tumor and the concentration of the fluorophore within it should allow the surgeon to make more informed decisions according to an objective risk-benefit assessment. The detection of residual cancer tissue at depths up to 5 to 10 mm beneath the surgical surface may result in a reduced volume of residual disease left behind post-operatively, which should impact positively on patient survival.

Acknowledgments

This work was supported by grants from the Fonds de recherche du Québec—Nature et technologies (FRQNT), the Natural Sciences and Engineering Research Council of Canada (NSERC), the Groupe de Recherche en Sciences et Technologies biomédicales (GRSTB), and the US National Institutes of Health (NIH) grant R01NS052274-01A2.

References

- M. J. McGirt et al., "Extent of surgical resection is independently associated with survival in patients with hemispheric infiltrating low-grade gliomas," *Neurosurgery* **63**(4), 700–708 (2008).
- W. Stummer et al., "Prospective cohort study of radiotherapy with concomitant and adjuvant temozolomide chemotherapy for glioblastoma patients with no or minimal residual enhancing tumor load after surgery," *J. Neurooncol.* **108**(1), 89–97 (2012).
- J. S. Smith et al., "Role of extent of resection in the long-term outcome of low-grade hemispheric gliomas," *J. Clin. Oncol. Off. J. Am. Soc. Clin. Oncol.* **26**(8), 1338–1345 (2008).
- L. Capelle et al., "Spontaneous and therapeutic prognostic factors in adult hemispheric World Health Organization Grade II gliomas: a series of 1097 cases: clinical article," *J. Neurosurg.* **118**(6), 1157–1168 (2013).
- A. L. Vahrmeijer et al., "Image-guided cancer surgery using near-infrared fluorescence," *Nat. Rev. Clin. Oncol.* **10**(9), 507–518 (2013).
- J. Regelsberger et al., "Ultrasound-guided surgery of deep seated brain lesions," *Eur. J. Ultrasound* **12**(2), 115–121 (2000).
- N. Sanai et al., "Intraoperative confocal microscopy in the visualization of 5-aminolevulinic acid fluorescence in low-grade gliomas," *J. Neurosurg.* **115**(4), 740–748 (2011).
- A. S. Haka et al., "In vivo margin assessment during partial mastectomy breast surgery using Raman spectroscopy," *Cancer Res.* **66**(6), 3317–3322 (2006).
- R. Richards-Kortum and E. Sevick-Muraca, "Quantitative optical spectroscopy for tissue diagnosis," *Annu. Rev. Phys. Chem.* **47**, 555–606 (1996).
- W. Stummer et al., "Fluorescence-guided resection of glioblastoma multiforme by using 5-aminolevulinic acid-induced porphyrins: a prospective study in 52 consecutive patients," *J. Neurosurg.* **93**(6), 1003–1013 (2000).
- A. Nabavi et al., "Five-aminolevulinic acid for fluorescence-guided resection of recurrent malignant gliomas: a phase II study," *Neurosurgery* **65**(6), 1070–1077 (2009).
- A. B. K. Roessler, "Intraoperative tissue fluorescence using 5-aminolevulinic acid (5-ALA) is more sensitive than contrast MRI or amino acid positron emission tomography ((¹⁸F)-FET PET) in glioblastoma surgery," *Neurol. Res.* **34**(3), 314–317 (2012).
- P. A. Valdés et al., "Quantitative fluorescence in intracranial tumor: implications for ALA-induced PpIX as an intraoperative biomarker," *J. Neurosurg.* **115**(1), 11–17 (2011).
- P. A. Valdés et al., "Quantitative, spectrally-resolved intraoperative fluorescence imaging," *Sci. Rep.* **2**, 798 (2012).
- P. A. Valdés et al., "Combined fluorescence and reflectance spectroscopy for in vivo quantification of cancer biomarkers in low- and high-grade glioma surgery," *J. Biomed. Opt.* **16**(11), 116007 (2011).
- P. A. Valdés et al., "System and methods for wide-field quantitative fluorescence imaging during neurosurgery," *Opt. Lett.* **38**(15), 2786–2788 (2013).
- F. Leblond et al., "Analytic expression of fluorescence ratio detection correlates with depth in multi-spectral sub-surface imaging," *Phys. Med. Biol.* **56**(21), 6823–6837 (2011).
- S. Luo et al., "A review of NIR dyes in cancer targeting and imaging," *Biomaterials* **32**(29), 7127–7138 (2011).
- S. Achilefu, "The insatiable quest for near-infrared fluorescent probes for molecular imaging," *Angew. Chem. Int. Ed.* **49**(51), 9816–9818 (2010).
- R. S. Bradley and M. S. Thorniley, "A review of attenuation correction techniques for tissue fluorescence," *J. R. Soc. Interface* **3**(6), 1–13 (2006).
- B. Brooksby et al., "Imaging breast adipose and fibroglandular tissue molecular signatures by using hybrid MRI-guided near-infrared spectral tomography," *Proc. Natl. Acad. Sci. U. S. A.* **103**(23), 8828–8833 (2006).
- S. C. Davis et al., "Magnetic resonance-coupled fluorescence tomography scanner for molecular imaging of tissue," *Rev. Sci. Instrum.* **79**(6), 064302 (2008).
- D. Kepshire et al., "A microcomputed tomography guided fluorescence tomography system for small animal molecular imaging," *Rev. Sci. Instrum.* **80**(4), 043701 (2009).
- Y. Lin et al., "Quantitative fluorescence tomography using a combined tri-modality FT/DOT/XCT system," *Opt. Express* **18**(8), 7835–7850 (2010).
- J.-P. L'huillier and F. Vaudelle, "Improved localization of hidden fluorescent objects in highly scattering slab media based on a two-way transmittance determination," *Opt. Express* **14**(26), 12915–12929 (2006).
- B. Yuan and Q. Zhu, "Separately reconstructing the structural and functional parameters of a fluorescent inclusion embedded in a turbid medium," *Opt. Express* **14**(16), 7172–7187 (2006).
- A. Laidevant et al., "Analytical method for localizing a fluorescent inclusion in a turbid medium," *Appl. Opt.* **46**(11), 2131–2137 (2007).
- D. S. Kepshire et al., "Subsurface diffuse optical tomography can localize absorber and fluorescent objects but recovered image sensitivity is nonlinear with depth," *Appl. Opt.* **46**(10), 1669–1678 (2007).
- V. Ntziachristos, C. Bremer, and R. Weissleder, "Fluorescence imaging with near-infrared light: new technological advances that enable in vivo molecular imaging," *Eur. Radiol.* **13**(1), 195–208 (2003).
- M. Hassan et al., "Fluorescence lifetime imaging system for in vivo studies," *Mol. Imaging* **6**(4), 229–236 (2007).
- M. Brambilla et al., "Time-resolved scanning system for double reflectance and transmittance fluorescence imaging of diffusive media," *Rev. Sci. Instrum.* **79**(1), 013103 (2008).
- K. M. Tichauer et al., "Imaging workflow and calibration for CT-guided time-domain fluorescence tomography," *Biomed. Opt. Express* **2**(11), 3021–3036 (2011).
- M. J. Niedre et al., "Early photon tomography allows fluorescence detection of lung carcinomas and disease progression in mice in vivo," *Proc. Natl. Acad. Sci. U. S. A.* **105**(49), 19126–19131 (2008).
- V. Ntziachristos et al., "Looking and listening to light: the evolution of whole-body photonic imaging," *Nat. Biotechnol.* **23**(3), 313–320 (2005).
- E. E. Graves, R. Weissleder, and V. Ntziachristos, "Fluorescence molecular imaging of small animal tumor models," *Curr. Mol. Med.* **4**(4), 419–430 (2004).
- D. Kepshire et al., "Fluorescence tomography characterization for subsurface imaging with protoporphyrin IX," *Opt. Express* **16**(12), 8581–8593 (2008).
- M. E. Eames et al., "Wavelength band optimization in spectral near-infrared optical tomography improves accuracy while reducing data acquisition and computational burden," *J. Biomed. Opt.* **13**(5), 054037 (2008).
- J. Swartling et al., "Fluorescence spectra provide information on the depth of fluorescent lesions in tissue," *Appl. Opt.* **44**(10), 1934–1941 (2005).
- B. W. Pogue et al., "Review of neurosurgical fluorescence imaging methodologies," *IEEE J. Sel. Topics Quantum Electron.* **16**(3), 493–505 (2010).
- A. D. Klose and T. Pöschinger, "Excitation-resolved fluorescence tomography with simplified spherical harmonics equations," *Phys. Med. Biol.* **56**(5), 1443–1469 (2011).

41. S. L. Jacques and B. W. Pogue, "Tutorial on diffuse light transport," *J. Biomed. Opt.* **13**(4), 041302 (2008).
42. K. Kolste et al., "A macroscopic optical imaging technique for wide-field estimation of fluorescence depth in optically-turbid media for application in brain tumor surgical guidance," *J. Biomed. Opt.* **20**(2), 026002 (2015).
43. M. Jermyn et al., "Fast segmentation and high-quality three-dimensional volume mesh creation from medical images for diffuse optical tomography," *J. Biomed. Opt.* **18**(8), 086007 (2013).
44. H. Dehghani et al., "Near infrared optical tomography using NIRFAST: algorithm for numerical model and image reconstruction," *Commun. Numer. Methods Eng.* **25**(6), 711–732 (2009).
45. S. C. Davis et al., "Image-guided diffuse optical fluorescence tomography implemented with Laplacian-type regularization," *Opt. Express* **15**(7), 4066–4082 (2007).
46. W. Zijlstra and A. Buursma, "Spectrophotometry of hemoglobin: absorption spectra of bovine oxyhemoglobin, deoxyhemoglobin, carboxyhemoglobin, and methemoglobin," *Comp. Biochem. Physiol. B Biochem. Mol. Biol.* **118**(4), 743–749 (1997).
47. R. Michels, F. Foschum, and A. Kienle, "Optical properties of fat emulsions," *Opt. Express* **16**(8), 5907–5925 (2008).
48. T. J. Farrell, M. S. Patterson, and B. Wilson, "A diffusion theory model of spatially resolved, steady-state diffuse reflectance for the noninvasive determination of tissue optical properties in vivo," *Med. Phys.* **19**(4), 879–888 (1992).
49. Q. Fang, "Mesh-based Monte Carlo method using fast ray-tracing in Plücker coordinates," *Biomed. Opt. Express* **1**(1), 165–175 (2010).
50. Q. Fang and D. R. Kaeli, "Accelerating mesh-based Monte Carlo method on modern CPU architectures," *Biomed. Opt. Express* **3**(12), 3223–3230 (2012).
51. M. Chu and H. Dehghani, "Image reconstruction in diffuse optical tomography based on simplified spherical harmonics approximation," *Opt. Express* **17**(26), 24208–24223 (2009).
52. K. M. Tichauer et al., "Dual-tracer background subtraction approach for fluorescence molecular tomography," *J. Biomed. Opt.* **18**(1), 016003 (2013).
53. D. J. Cuccia et al., "Quantitation and mapping of tissue optical properties using modulated imaging," *J. Biomed. Opt.* **14**(2), 024012 (2009).
54. B. Yang, M. Sharma, and J. W. Tunnell, "Attenuation-corrected fluorescence extraction for image-guided surgery in spatial frequency domain," *J. Biomed. Opt.* **18**(8), 080503 (2013).
55. A. J. Chaudhari et al., "Excitation spectroscopy in multispectral optical fluorescence tomography: methodology, feasibility and computer simulation studies," *Phys. Med. Biol.* **54**(15), 4687–4704 (2009).
56. A. Johansson et al., "5-aminolevulinic acid-induced protoporphyrin IX levels in tissue of human malignant brain tumors," *Photochem. Photobiol.* **86**(6), 1373–1378 (2010).
57. R. Ishihara et al., "Quantitative spectroscopic analysis of 5-aminolevulinic acid-induced protoporphyrin IX fluorescence intensity in diffusely infiltrating astrocytomas," *Neurol. Med. Chir. (Tokyo)* **47**(2), 53–57 (2007).

Biographies of the authors are not available.